Browse Journals & Magazines > IEEE Sensors Journal

IEEE Sensors Journal

4.5 Impact Factor	**0.06589** Eigenfactor
0.746 Article Influence Score	**8.2** CiteScore

Powered by Scopus

Submit Manuscript

Submission Guidelines

Become a Reviewer

Open Access Publishing Options

Add Title To My Alerts

Add to My Favorites

Home | Popular | Early Access | Current Issue | All Issues | About Journal

Aims & Scope

According to the IEEE Sensors Council's constitution, "The fields of interest of the Council and its activities shall be the theory, design, fabrication, manufacturing and application of devices for sensing and transducing physical, chemical, and biological phenomena, with emphasis on the electronics and physics aspects of sensors and integrated sensor-actuators." The *IEEE Sensors Journal* focuses on the numerous sensor technologies spanned by the IEEE, and on emerging sensor technologies.

Publication Fees

This publication is hybrid, meaning that it is supported by subscriptions and applicable article processing charges (APCs). Although there is no cost for publishing with IEEE, authors may wish to take advantage of some of our fee-based offerings, for example, choosing to publish open access in a hybrid journal. Visit the IEEE Author Center for more information on available options. The open access APC for this title is **$2,800 USD**. Learn more

Contact Information

Editor-in-Chief

Zeynep Celik
University of Texas at Arlington
Arlington
USA
zcelik@uta.edu

Editorial Board

Author Center

IEEE Sensors Journal

Popular | Recent | Most Cited

Information for Authors

Publishing Policies

A Lightweight Perception Enhancement Network For Real-Time And Accurate Internal Surface Defect Detection Of Cold-Drawn Steel Pipes

You Tan; Kechen Song; Hongshu Chen; Yu Zhang; Yunhui Yan

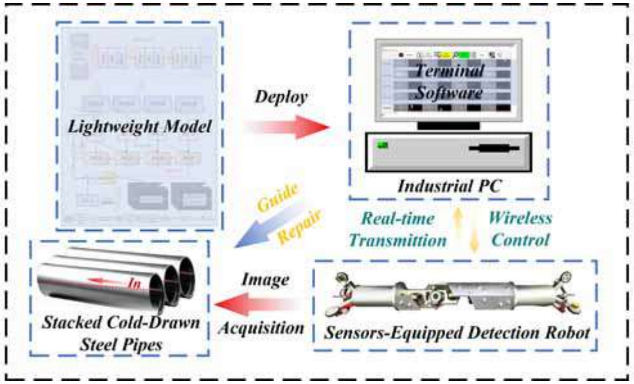

Smart Insoles With Textile Capacitive Sensors For Efficient Gait Phase Recognition

Panagiotis Mavrogiannis; Ilias Maglogiannis; Lazar Milić; Christos Panagopoulos; Andreas Menychtas; Goran M. Stojanović

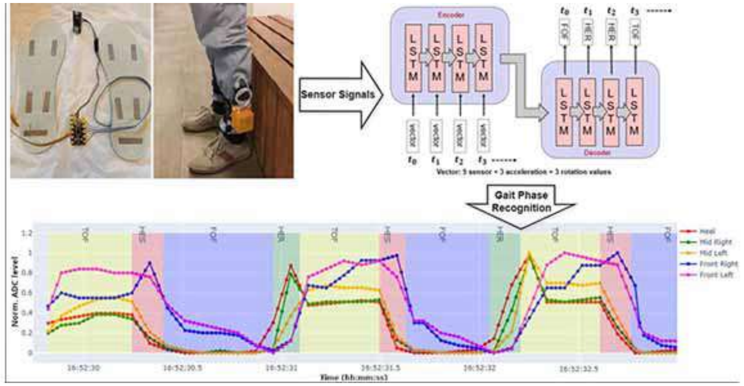

Unified Neural Network-Based Shape Sensing For Continuum Robots Using Fiber Bragg Gratings

Samuel Wild; Belal A. Elsayed; Hongshen Shi; Simon D. Jones; Tianyi Zeng; Abdelkhalick Mohammad; Dragos Axinte; Xin Dong

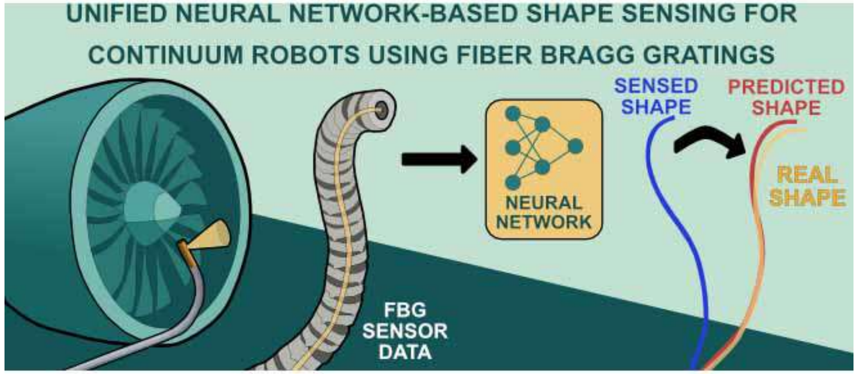

Silicon–Platinum Bowtie-Coupled Thermoelectric Terahertz Detector

Francisco Javier González; Robert E. Peale; Juan R. Moreno

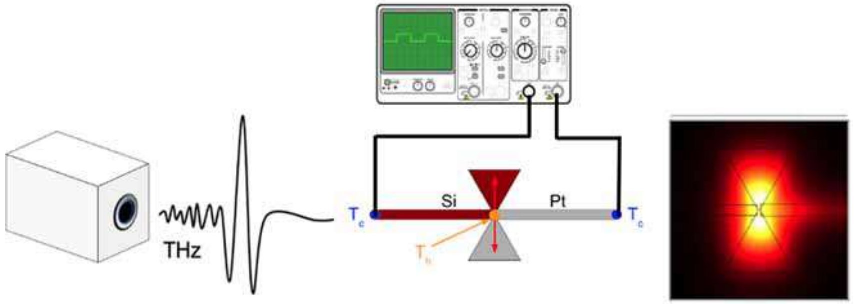

3D-Printed Airflow Hair Sensor Inspired By The Buthus Occitanus Scorpion’s Flat Trichobothria

Samuele Martinelli; Andrew Reid; James F. C. Windmill

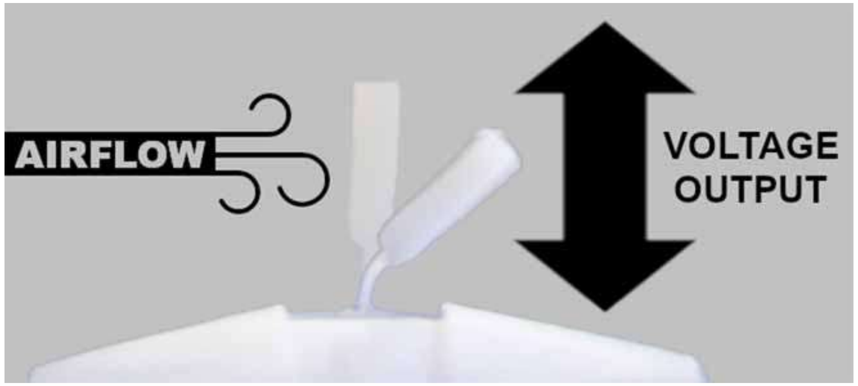

Show All

Related Magazines or Journals

IEEE Transacti
Components, Pa
and Manufac
Technolog

IEEE Access

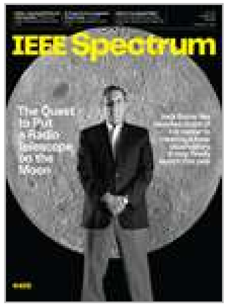

IEEE Spectrum

IEEE Personal Account

CHANGE USERNAME/PASSWORD

Purchase Details

PAYMENT OPTIONS

VIEW PURCHASED DOCUMENTS

Profile Information

COMMUNICATIONS PREFERENCES

PROFESSION AND EDUCATION

TECHNICAL INTERESTS

Need Help?

US & CANADA: +1 800 678 4333

WORLDWIDE: +1 732 981 0060

CONTACT & SUPPORT

Follow

About IEEE *Xplore* | Contact Us | Help | Accessibility | Terms of Use | Nondiscrimination Policy | IEEE Ethics Reporting | Sitemap | IEEE Privacy Policy

A public charity, IEEE is the world's largest technical professional organization dedicated to advancing technology for the benefit of humanity.

Journals & Magazines > IEEE Sensors Journal > Volume: 26 Issue: 4

High-Q H-Shaped Nested Split-Ring Resonator Sensor for Liquid Complex-Permittivity Characterization

Publisher: IEEE

Cite This PDF

Muhamad Zaki Abdul Rahman ; Muhammad Idzdihar Idris ; Nazrin Haziq Jemaludin ; Md Razip Bin Mat ; Safpbri Johari ; Syah Alam All Authors

Abstract:
We present a single-layer, via-less H-shaped nested split-ring resonator (H-NSRR) for complex-permittivity characterization of small-volume liquids. A square ring with a central H-slot colocates the electric and magnetic fields in the same gap, improving frequency resolution and sensitivity while preserving a high unloaded Q. At around 5.9 GHz, the prototype achieves an unloaded Q of 346 in air and a normalized frequency sensitivity of approximately 1.19% per unit change in ε_r' , using an open PET tray (0.5 mL) positioned over the peak-|E| region to avoid microfluidic channels, vias, and multilayer processing. An equivalent-circuit model and an empirical retrieval framework map resonance-frequency shifts and Q-factor variations to the real and imaginary parts of permittivity, with retrieved values in close agreement with full-wave simulations and benchtop measurements. The proposed sensor combines high sensitivity, high unloaded Q, repeatable small-volume handling, and single-layer manufacturability, making it a practical platform for compact, application-ready microwave material characterization.

Figures

References

Keywords

Metrics

More Like This

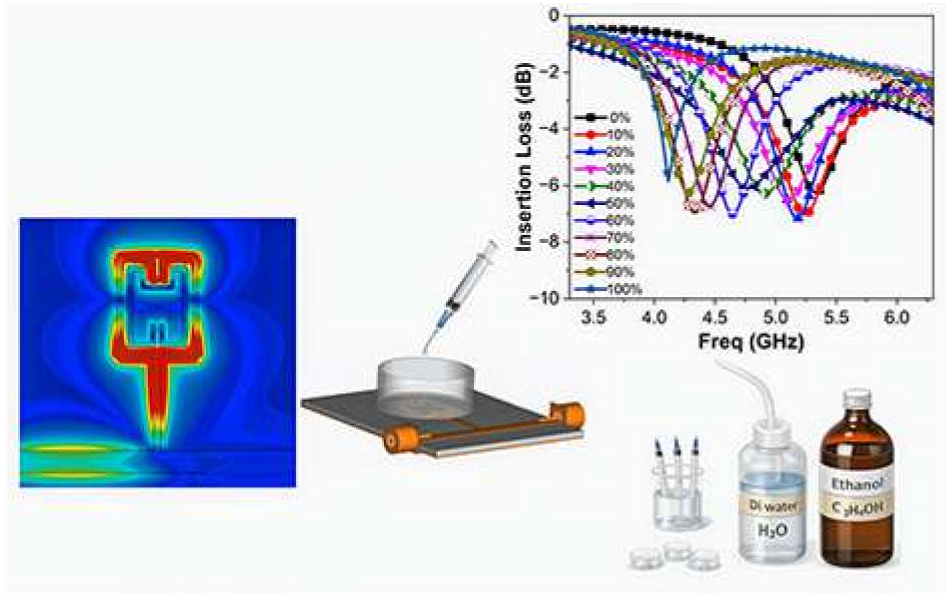

Published in: IEEE Sensors Journal (Volume: 26 , Issue: 4, 15 February 2026)

Page(s): 5510 - 5518

DOI: 10.1109/JSEN.2025.3648960

Date of Publication: 12 January 2026

Publisher: IEEE

ISSN Information:

I. Introduction

The performance of modern RF, wireless, and sensing systems is intrinsically linked to the electromagnetic behavior of their constituent materials, which is fundamentally governed by permittivity and permeability [1], [2]. Permittivity, in particular, serves as a critical indicator of electromagnetic response due to its strong frequency dependence in the RF and microwave regime [1]. Since dielectric behavior is directly correlated with material quality [3], obtaining accurate permittivity data ... applications in aerospace, chemical sensing, and communication systems [4]. Motivated by the need for compact, application-ready measurements,

Sign in to Continue Reading

Authors

Figures

References

Keywords

Metrics

High-Q H-Shaped Nested Split-Ring Resonator Sensor for Liquid Complex-Permittivity Characterization

Muhamad Zaki Abdul Rahman*, Muhammad Idzdihar Idris, Nazrin Haziq Jemaludin, Md Razip Mat, Safpbri Johari, Syah Alam and Zahriladha Zakaria*, *Senior Member, IEEE*

***Abstract*— We present a single-layer, via-less H-shaped nested split-ring resonator (H-NSRR) for complex-permittivity characterization of small-volume liquids. A square ring with a central H-slot co-locates the electric and magnetic fields in the same gap, improving frequency resolution and sensitivity while preserving a high unloaded Q. At around $5.9\,\mathrm{GHz}$, the prototype achieves an unloaded Q of 346 in air and a normalized frequency sensitivity of approximately 1.19% per unit change in ε_r', using an open PET tray ($0.5\,\mathrm{mL}$) positioned over the peak-$|\mathbf{E}|$ region to avoid microfluidic channels, vias, and multilayer processing. An equivalent-circuit model and an empirical retrieval framework map resonance-frequency shifts and Q-factor variations to the real and imaginary parts of permittivity, with retrieved values in close agreement with full-wave simulations and benchtop measurements. The proposed sensor combines high sensitivity, high unloaded Q, repeatable small-volume handling, and single-layer manufacturability, making it a practical platform for compact, application-ready microwave material characterization.**

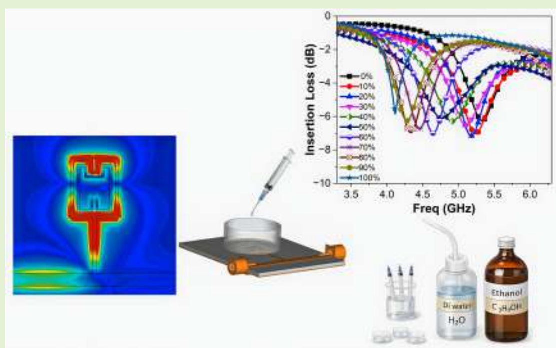

***Index Terms*— H-shaped nested split-ring resonator (H-NSRR), microwave resonator sensors, complex-permittivity retrieval, small-volume liquid characterization, open-tray sample handling**

I. Introduction

THE performance of modern RF, wireless, and sensing systems is intrinsically linked to the electromagnetic behavior of their constituent materials, which is fundamentally governed by permittivity and permeability [1], [2]. Permittivity, in particular, serves as a critical indicator of electromagnetic response due to its strong frequency dependence in the RF and microwave regimes [1]. Since dielectric behavior is directly correlated with material quality [3], obtaining accurate permittivity data is essential for advancing applications in aerospace, chemical sensing, and communication systems [4]. Motivated by the need for compact, application-ready measurements, recent work has focused on planar resonant implementations that offer high resolution with fabrication-friendly layouts [5], [6].

Planar microwave sensors have consequently become a leading platform for dielectric testing [7]. They are widely used for antenna tuning and integrate readily with ISM-band subsystems [8]. Their low cost, non-invasive operation, and real-time capability support applications from blood-glucose monitoring [9] and displacement sensing [10] to food safety inspection [11], structural health monitoring [12], environmental detection [13], and complex-permittivity characterization of liquids for chemical composition analysis [14]–[24].

To intensify field localization and sensitivity, many resonant topologies have been explored, including interdigital capacitors [25], coplanar waveguides [26], high-directivity microstrip coupled-line directional couplers [27], step-impedance resonators [28], metamaterial split-ring and complementary split-ring resonators [29], and hairpin open-loop resonators [30]. Active circuitry has been used to compensate loss [31], and diverse liquid-handling schemes have been developed for chemical and biofluid characterization [32]. These enhancements often improve one aspect while degrading another: stronger localization can increase sensitivity but complicates fabrication; microfluidic precision stabilizes loading but can lower Q through added dielectric loss; multilayer routing introduces vias and alignment steps that raise cost and reduce portability.

Representative SRR-based designs illustrate these advances and trade-offs. A differential hexagonal-SRR pair [33] improves common-mode rejection for liquid-permittivity sensing while maintaining a compact $30 \times 22\ \mathrm{mm}^2$ footprint. An active-feedback SRR with an embedded microfluidic channel [34] reports $Q \approx 13{,}000$ and fine resolution but increases system complexity and reduces portability. A configuration combining a defected ground structure, interdigital capacitors, and a dual SRR beneath a PDMS microfluidic chip [35] yields larger frequency shifts. However, attaching or filling the chip or channel lowers the notch depth and shifts the resonance. The

Received XXX; revised XXX; accepted XXX. Date of publication XXX; date of current version XXX.

M. Z. A. Rahman, Z. Zakaria, M. I. Idris, and N. H. Jemaludin are with the CeTRI, FKEKK, UTeM, Melaka, Malaysia.
M. Z. A. Rahman, M. R. Mat, and S. Johari are with the Dep. of Electrical Engineering, PUO, Perak, Malaysia.
S. Alam is with the Dep. of Electrical Engineering, Universitas Trisakti, Jakarta, Indonesia.
Corresponding authors: Muhamad Zaki Abdul Rahman (zakiman@puo.edu.my) and Zahriladha Zakaria (zahriladha@utem.edu.my).

This article has been accepted for publication in IEEE Sensors Journal. This is the author's version which has not been fully edited and content may change prior to final publication. Citation information: DOI 10.1109/JSEN.2025.3648960

measurements use stop-flow and drying steps, require vias, and the measured Q is modest, in the range of 50–98. An asymmetric SRR cavity in a metal–insulator–metal waveguide [36] produces multiple Fano resonances for high-resolution sensing, though nanoscale multilayer fabrication with tight alignment tolerances is required. Finally, a dual-band SRR with an integrated microfluidic channel [37] can sense both liquid permittivity and solid displacement, at the cost of added fabrication steps and more involved two-port coupling and isolation.

Beyond individual exemplars, comparative reports highlight recurring trade-offs that still hinder wider deployment. Even with high unloaded Q, resonators can exhibit small normalized shifts for low-dispersion liquids (about 0.30% in liquids), which limits responsiveness to subtle permittivity changes [16]. Analyses also indicate intrinsic sensitivity limits in planar SRR/CSRR topologies, and common remedies such as IPD implementations or aggressively boosting Q raise design and fabrication complexity and cost [38]. Sustainability-minded substrates are promising but tend to exhibit higher dielectric loss, which lowers Q and makes retrieval more difficult [39]. Hybrid DGS–IDC–DSRR layouts can increase relative frequency shift and notch depth, yet they rely on backside DGS and via drilling (four vias), adding steps beyond a simple single-layer sensor [35]. Low-cost FR-4 CSRR implementations remain attractive but explicitly accept lower Q, which leads to broader resonances and reduced spectral resolution, while contactless "tube-on-top" handling (a capillary normal to the ground) keeps fabrication simple [19]. Finally, metamaterial-assisted couplers can boost sensitivity and stabilize coupling across materials under test (MUTs), but this comes at the cost of additional circuitry [40].

To address these limitations, we propose a compact single-layer via-less H-shaped nested split ring resonator (H-NSRR) that colocates the electric and magnetic fields in the same sensing gap, preserving high unloaded Q and sharpening spectral resolution. A square ring with a central H slot concentrates both fields at one location; an open PET tray (0.5 mL) placed over the peak $|\mathbf{E}|$ region loads liquids without microfluidic channels, vias, or multilayer steps, reducing dielectric loss and simplifying fabrication. An equivalent circuit model together with an empirical retrieval framework maps resonance frequency shifts and Q variations to ε_r' and ε_r'', with results closely matching full-wave simulations and bench measurements, making the sensor practical for compact, application-ready microwave material characterization.

The main contributions of this work are as follows: (i) a single-layer, via-less H-NSRR that co-localizes fields in the sensing gap while preserving a high unloaded quality factor Q_u; (ii) an open-tray (0.5 mL) liquid-handling method that removes microfluidic losses and fabrication overhead; and (iii) validated empirical models for ε_r' and ε_r'' derived from frequency and Q responses, matching full-wave simulations and measurements. Together, these features yield a via-less H-NSRR that, unlike prior single-layer SRR/CSRR liquid sensors [14]–[19], offers high Q_u and normalized sensitivity S_n with simple open PET-tray loading in a single structure. The paper is organized as follows: Section II presents the sensor design and parameter optimization; Section III develops the resonance modeling (equivalent-circuit, field characteristics, perturbation-based retrieval, and Q definitions); Section IV describes fabrication and measurement; Section V reports results and benchmarking; and Section VI concludes the work.

II. Design of the Sensor

A. H-NSRR Geometry and Parameter Optimization

The proposed H-shaped nested split-ring resonator (H-NSRR) consists of a square microstrip ring with a central horizontal H-slot. The ring path provides inductance and the two slot gaps act as an effective series capacitance, so the overall response follows an LC resonance. In canonical SRRs, electric energy is stored predominantly near the split gap while magnetic energy is concentrated in the loop interior; this motivates co-locating both fields within the same sensing gap to raise responsiveness while keeping a sharp notch [41].

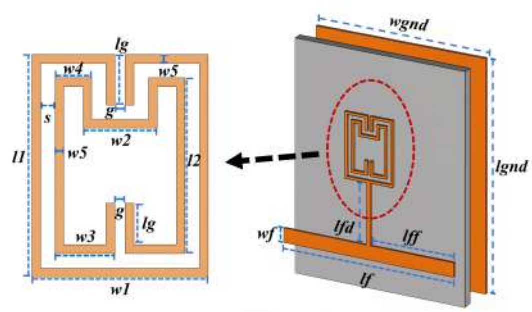

Fig. 1. Annotated top view and layer stack-up of the proposed H-NSRR.

A 50 Ω microstrip feed is side-coupled across the coupling gap s to set the external loading and the notch depth. Figure 1 shows the annotated top view and the layer stack-up. Dimension symbols are used consistently throughout the paper: l_1 (outer ring length), w_1 (outer ring width), w_2 (H-slot width), l_2 (inner ring length), w_3/w_4 (left/right H-arm widths), w_5 (narrow trace width), l_g (horizontal gap length), g (slot gap), and s (coupling gap to the 50 Ω line).

TABLE I

Optimized H-NSRR Geometry and Functions.

Physical Parameter	Symbol (Name)	Value (mm)	Technical Function
Outer/Inner ring length	l_1/l_2	10.7	Tune inductive path and f_r
Outer ring width	w_1	8.5	Main current path; series resistance
H-slot width	w_2	3.6	Field-concentration zone
H-arm widths (left/right)	w_3/w_4	2.9 / 1.8	Horizontal current paths; affect Q_u
Narrow trace width	w_5	0.42	Controls series resistance/ current density
Horizontal gap length	l_g	2.42	Sets horizontal slot length
Slot gap	g	0.4	Sensing-gap capacitance; field confinement
Coupling gap	s	0.4	Sets Q_e and notch depth/width
Feed line length/width	l_f/w_f	30 / 2	50 Ω microstrip (RO5880)
Feed segments / transitions	l_{fd}/l_{ff}	29 / 8	Path to port / width transition
Ground-plane length/width	$l_{\text{gnd}}/w_{\text{gnd}}$	40 / 30	Board dimensions

The coupling gap s governs the external quality factor Q_e and therefore the coupling strength. Reducing s strengthens coupling and deepens the $|S_{21}|$ notch while widening it; enlarging s weakens coupling and narrows the notch but makes it shallower. Under near-critical conditions, with coupling factor β close to 1, internal and external losses balance, producing a deep and spectrally sharp notch. We use the standard relations $Q_u = Q_l(1+\beta) = \beta Q_e$ and the critical-coupling criterion for quality-factor extraction [42].

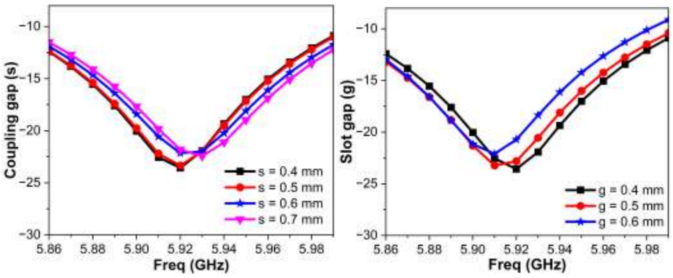

(a) (b)

Fig. 2. Simulated responses of the proposed H-NSRR: (a) coupling gap s sweep; (b) slot gap g sweep.

The slot gap g sets the effective capacitance and the degree of electric-field concentration in the sensing region. Decreasing g increases capacitance and raises the stored electric energy fraction in the gap, which amplifies the frequency shift per unit change in ε_r'; for lossy liquids, even a very small gap can significantly reduce Q_u. Increasing g reduces sensitivity but stabilizes the notch depth. The widths w_3/w_4 and w_5 shape current density and series resistance, influencing Q_u, while l_1 and l_2 tune the inductive path and set f_r. The PET tray height is chosen to maximize field–sample overlap without parasitic loading. Figure 2(b) shows the g sweep and the resulting sensitivity–Q tradeoff, consistent with the well-known partitioning of electric and magnetic energy in SRR structures [41].

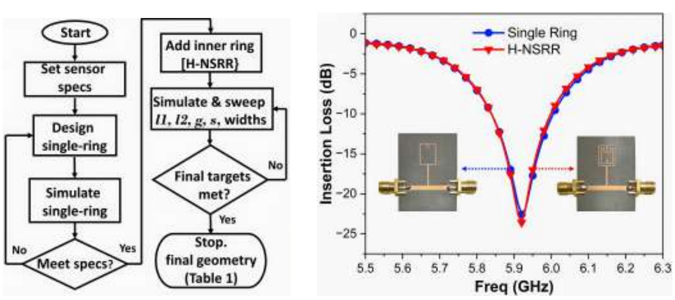

(a) (b)

Fig. 3. (a) Design flowchart of the proposed H-NSRR sensor; (b) measured $|S_{21}|$ of H-SRR and H-NSRR prototypes.

The dimensioning procedure that produces the values in Table I follows the flowchart in Fig. 3(a). Starting from a single-ring H-SRR template, l_1, l_2, g, s, and the trace widths are iteratively tuned until the 5.9-GHz resonance and target unloaded Q-factor are achieved. Figure 3(b) then compares the measured $|S_{21}|$ responses of the initial single-ring H-SRR and the final double-ring H-NSRR prototypes, highlighting the change in transmission between these design stages.

III. Resonance Modeling and Sensing Principle

A. Lumped Element Model and Validation

The H-NSRR is modeled as a parallel LC tank capacitively coupled to a $50\ \Omega$ microstrip line (Fig. 4). The loop inductance L_s follows the current path along the outer ring and the H arms, while the two slot gaps are represented as series capacitors $C/2$. According to the series-gap mapping, this pair is replaced by an effective series capacitance C_s [43]. With these elements, the resonance frequency is

$$f_r = \frac{1}{2\pi\sqrt{L_s C_s}}. \quad (1)$$

The resistance R accounts for conductor, dielectric, and radiation losses. A small element at the port emulates the feeding condition and adjusts the external coupling. Using the optimized values $L_s = 0.4371$ nH and $C_{\text{total}} = 6.62$ pF (so $C_s = 1.655$ pF), the predicted f_r agrees with full-wave simulation and measurement within about 1%. Figure 4 shows the lumped-element equivalent circuit model used throughout this section.

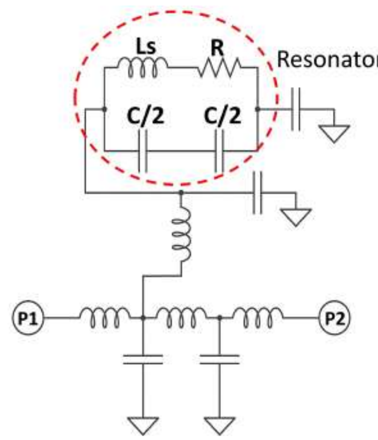

Fig. 4. Lumped-element equivalent circuit of the proposed H-NSRR sensor.

B. Field Confinement and Mode Structure

Full-wave simulations reveal that the H-slot effectively concentrates the electromagnetic fields within the narrow sensing gap (Fig. 5(a)). The peak electric-field magnitude $|\mathbf{E}|$ is localized along the slot edges, while the square-ring path forms the inductive loop that stores magnetic energy. Quantitatively, the peak $|\mathbf{E}|$ in the sensing gap reaches 1.44×10^4 V/m, exceeding the surrounding field by approximately one order of magnitude.

This intense confinement within the sample volume maximizes the frequency shift governed by the perturbation model [41], [44]. At the same time, the surface-current density in Fig. 5(b) exhibits closed anti-parallel circulation loops along the outer ring and the inner H-shaped arms. This current distribution spatially coincides with the high $|\mathbf{E}|$ region. Consistent with split-ring resonator theory, the electric energy is concentrated near the gaps while the magnetic energy is stored in the loops, and the shortened side arms in this design suppress the magnetic response and remove the net magnetic moment [41].

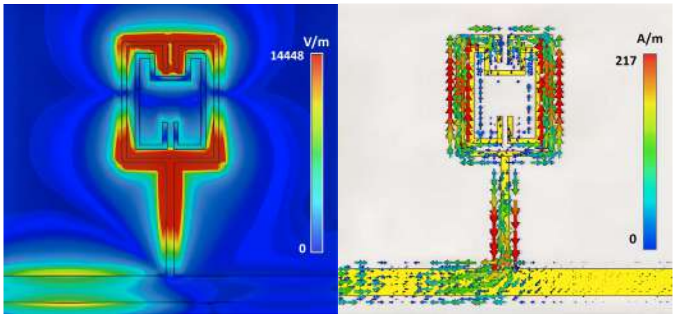

(a) (b)

Fig. 5. Field confinement at resonance: (a) localized electric-field intensity $|\mathbf{E}|$; (b) closed-loop surface-current distribution $|\mathbf{J}|$.

C. Perturbation Theory for Liquid Loading

When a liquid sample is placed in the strong-$\mathbf{E}$ region, the stored energy of the resonant mode changes and the resonance shifts. For small perturbations, the complex fractional shift can be written in the energy-weighted form [44]

$$\frac{\Delta\omega}{\omega_r} = \frac{\int_{V_{\mathrm{MUT}}} (\Delta\varepsilon |E_0|^2 - \Delta\mu |H_0|^2)\, dv}{\int_v (\varepsilon_0 |E_0|^2 + \mu_0 |H_0|^2)\, dv} = \frac{\int_{V_{\mathrm{MUT}}} (\Delta\varepsilon |E_0|^2 - \Delta\mu |H_0|^2)\, dv}{2\int_v \varepsilon_0 |E_0|^2\, dv} \tag{2}$$

The real part maps to the frequency shift, while the imaginary part maps to the change in $1/Q$ [44]. For non-magnetic liquids ($\Delta\mu \approx 0$), the electric-energy filling factor is

$$\rho_E = \frac{\int_{V_{\mathrm{MUT}}} \varepsilon_0 |E_0|^2\, dv}{\int_v \varepsilon_0 |E_0|^2\, dv} \tag{2a}$$

which is equivalent to the energy constant used in cavity-perturbation derivations [44].

Under weak loading, with $\Delta\varepsilon = \varepsilon_{\mathrm{MUT}} - \varepsilon_{\mathrm{bg}}$ and neglecting $\Delta\mu$, the working relation becomes

$$\frac{\Delta f}{f_r} \approx -\frac{\rho_E}{2}\,\frac{\Delta\varepsilon_r'}{\varepsilon_{\mathrm{eff}}} \tag{3}$$

where $\varepsilon_{\mathrm{eff}}$ denotes the effective permittivity seen by the mode [44].

Following [3], [23], [24], the frequency-detection resolution (FDR) of the sensor is defined identically to the absolute sensitivity in (4), namely as the resonance-frequency shift per unit change in ε_r':

$$\mathrm{FDR} = \frac{\Delta f_r}{\Delta\varepsilon_r'} = S_a. \tag{4}$$

and the normalized sensitivity, where f_0 is the baseline resonance in air [3], [5],

$$S_n = \frac{\Delta f_r / f_0}{\Delta\varepsilon_r'} \times 100(\%). \tag{5}$$

D. Q-Factor Definitions (stopband)

In a stopband resonator, the 3-dB bandwidth $\Delta f_{\mathrm{3dB}} = f_2 - f_1$ is measured with respect to the notch minimum of $|S_{21}|$ [5]. The unloaded quality factor is then

$$Q_u = \frac{2 f_0}{\Delta f_{\mathrm{3dB}}}. \tag{6}$$

Unless stated otherwise, Q denotes Q_u. For a two-port resonator the factors satisfy $1/Q_l = 1/Q_u + 1/Q_e$; near critical coupling ($\beta \approx 1$) this gives $Q_l \approx Q_u/2$ [42], [45]. The dielectric loss of the sample is characterized by the loss tangent,

$$\tan\delta = \frac{\varepsilon_r''}{\varepsilon_r'}. \tag{7}$$

This relation links the imaginary part of permittivity to dissipation in the resonator response [4].

IV. Fabrication and Experimentation Setup

The H-NSRR was fabricated on Rogers RO5880 substrate ($\varepsilon_r = 2.2$, low-loss tangent $\tan\delta = 0.0027$, $h = 0.79$ mm) using standard photolithography followed by wet etching. A 35-μm copper layer on the top surface defined the resonator and the 50-Ω microstrip feed, while the bottom surface was retained as a continuous ground plane to ensure electromagnetic shielding and to suppress radiation leakage. PCB-mount SMA connectors were soldered at both ends of the feedline to provide matched transitions for two-port measurements. The fabricated prototype is shown in Fig. 6.

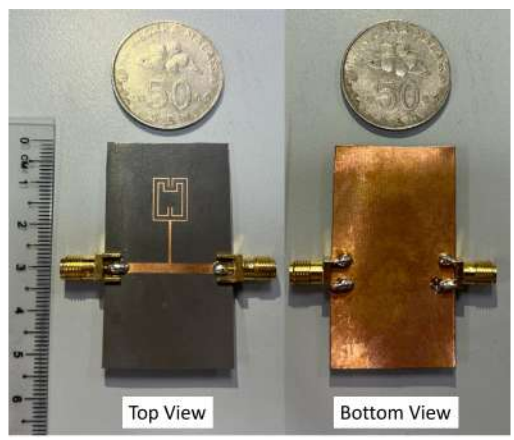

Fig. 6. Fabricated H-NSRR prototype.

Liquid samples were introduced using a thin-walled cylindrical PET (polyethylene terephthalate) tray (inner diameter approximately 15–16 mm, inner height about 10 mm, wall thickness 0.1 mm) positioned directly above the sensing slot, aligned with the region of maximum electric-field intensity predicted by simulation. A controlled volume of 0.5 mL was dispensed into the tray for each run using a syringe to maintain repeatability across materials under test. A parametric volume analysis confirmed that, for sample volumes between 0.5 mL and 1.0 mL, the resonance frequency varies by only about 10 MHz (approximately 0.2%); consequently, 0.5 mL was adopted as the operating volume to minimize errors due to minor handling variations. A small piece cut from the same tray was characterized using an Agilent 85070E dielectric-probe kit; at 5.9 GHz the PET exhibited $\varepsilon_r' \approx 2.11$ and $\varepsilon_r'' \approx 0.0085$ ($\tan\delta \approx 0.004$), confirming a low-permittivity, low-loss holder with only a minor influence on the sensor response compared with the liquids under test. The arrangement of the PET tray over the resonator is illustrated in Fig. 7.

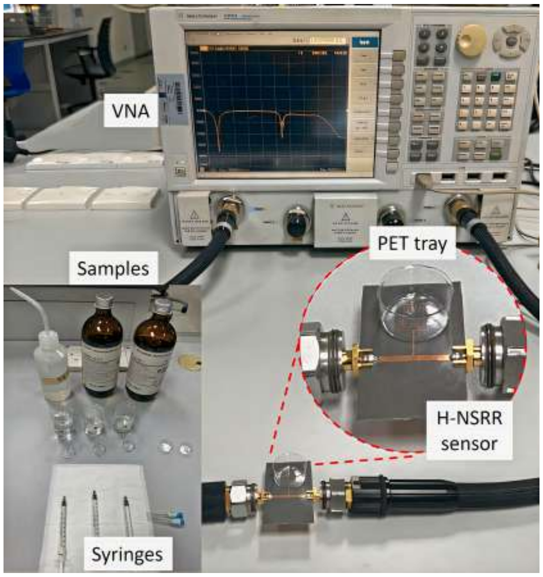

Fig. 7. VNA setup, H-NSRR sensor with PET tray, and calibration liquids with syringes.

Transmission measurements were conducted using an Agilent PNA-X N5242A vector network analyzer following a full two-port SOLT calibration. Sweep parameters (frequency span, number of points, source power, and IF bandwidth) were kept identical across all runs to ensure consistency. Measurement repeatability was validated through independent re-positioning trials of the empty PET tray; the resonance frequency at 5.833 GHz remained unchanged within the sweep's frequency resolution, confirming stable VNA calibration and fixture positioning. For dielectric benchmarking, an Agilent 85070E dielectric-probe kit was employed at frequencies close to the sensor resonance. The complete experimental setup, including the dispensing syringe, PET tray, and H-NSRR, is shown in Fig. 7 together with a representative $|S_{21}|$ trace.

V. Results and Discussion

A. Resonance and Dielectric Retrieval

To benchmark the response of the proposed sensor, Fig. 8(a) overlays the measured $|S_{21}|$ with the CST full-wave and the lumped-element responses. The three traces align in resonance and in the curvature near the notch minimum, indicating that the field distribution and coupling are captured consistently by both models. Residual differences away from the notch arise from cable/connector losses not included in the lumped model and from finite-size/dispersion effects in the PCB. This supports extracting Q via (6) and proceeding with dielectric retrieval on the measured trace.

With resonance validated, the measured resonance frequency is mapped to the real permittivity ε_r' using a calibrated quadratic relation. Air, ethanol, methanol, and deionized water span a wide ε_r' range. Fig. 8(b) shows a downward shift from 5.833 GHz (air) to 4.114 GHz (water), a 1.791 GHz span consistent with LC/perturbation theory because higher permittivity increases effective capacitance and lowers the resonant frequency. The resonance order, from highest to lowest frequency, is air, ethanol, methanol, and water. Higher-loss liquids exhibit broader, shallower notches, indicating larger ε_r'' and a lower Q_l.

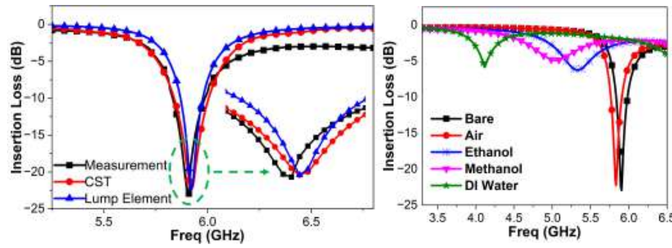

(a) (b)

Fig. 8. (a) Measured, CST-simulated, and lumped $|S_{21}|$ (benchmark resonance); (b) measured $|S_{21}|$ for the bare sensor and reference liquids.

Based on the calibration set $\{(f_r, \varepsilon_r')\}$ for air, ethanol, methanol, and deionized water, a second-order polynomial regression is used to model the nonlinear relationship between permittivity and resonance frequency, yielding the empirical mapping in (8), in line with similar curve-fitting strategies for liquid permittivity extraction [46].

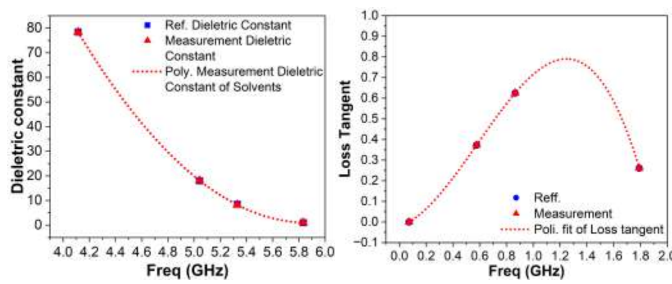

(a) (b)

Fig. 9. (a) Retrieved ε_r' vs. frequency with quadratic fit; (b) retrieved vs. reference $\tan\delta$ vs. frequency.

The fitted mapping is

$$\varepsilon_r' = 25.207\, f^2 - 295.72\, f + 868.33, \tag{8}$$

where f is in GHz. The regression in (8) matches the discrete reference points in Fig. 9(a) with $R^2 \approx 0.99994$. The mapping is strictly decreasing over $4.1 \leq f \leq 5.86$ GHz, enabling one-to-one inversion from f_r to ε_r'. At $f = 5.329$ GHz (ethanol), the local slope of (8) is $|\partial\varepsilon_r'/\partial f| \approx 27.06$ per GHz; with $\delta f = 1$ MHz this yields $\sigma_{\varepsilon_r'} \approx 0.027$ (absolute units of ε_r'). This is an uncertainty estimate from frequency resolution, not the percentage error in (9).

Following [20], we report the absolute relative error and its complement, accuracy:

$$\text{Error } (\%) = \frac{|V_{\text{ret}} - V_{\text{ref}}|}{V_{\text{ref}}} \times 100, \tag{9}$$

where V denotes the retrieved quantity (ε_r' or $\tan\delta$). Applying (8)–(9), the maximum error is 3.48% (air), the minimum is 0.04% (water), and the mean error is 1.77%, corresponding to an average accuracy of about 98% (Table II).

This article has been accepted for publication in IEEE Sensors Journal. This is the author's version which has not been fully edited and content may change prior to final publication. Citation information: DOI 10.1109/JSEN.2025.3648960

TABLE II
RESONANCE FREQUENCIES, FREQUENCY SHIFTS, AND REFERENCE VS. RETRIEVED PERMITTIVITIES.

LUT	Resonance Freq. (GHz)	Freq. Shift (GHz)	Ref. ε_r'	Retrieved ε_r'	Error (%)	Accuracy (%)
Air	5.833	N/A	1.0006	1.04	3.48	96.52
Ethanol	5.329	0.576	8.50	8.27	2.68	97.32
Methanol	5.041	0.864	18.00	18.16	0.88	99.12
DI Water	4.114	1.791	78.40	78.37	0.04	99.96

In resonant dielectric sensing, the imaginary part ε_r'' quantifies dissipation and appears as a broader, shallower notch; the loss tangent is defined as $\tan\delta = \varepsilon_r''/\varepsilon_r'$. Similarly, a cubic polynomial regression between the measured frequency shift Δf and the reference loss tangent $\tan\delta$ of the same calibration liquids is applied to obtain the empirical model in (10), following established polynomial loss-tangent retrieval methods [46]:

$$\tan\delta = -0.7064\,|\Delta f|^3 + 1.2394\,|\Delta f|^2 + 0.2036\,|\Delta f| - 0.0208 \quad (10)$$

Predictions for small Δf near zero are clipped to 0 for air; the fit is intended only for 4.1 to 5.86 GHz. Using (10), the measured Δf values were converted to $\tan\delta$ for each medium. Figure 9(b) shows retrieved $\tan\delta$ closely tracking independent references across the band. Table III summarizes the loss–tangent retrieval for the four liquids, with $\tan\delta$ obtained from (10) computed by (9). The maximum absolute error is 0.02%, and all cases exceed 99.98% accuracy, indicating a robust, repeatable loss extraction.

TABLE III
LOSS–TANGENT RETRIEVAL ACCURACY FOR PURE LIQUIDS.

LUT	f_r (GHz)	Δf (GHz)	$\tan\delta$ (ref.)	$\tan\delta$ (retr.)	Error (%)	Accuracy (%)
Air	5.833	N/A	0.0000	0.00004	0.00	99.938
Ethanol	5.329	0.576	0.37265	0.37270	0.01	99.994
Methanol	5.041	0.864	0.62465	0.62470	0.01	99.993
DI Water	4.114	1.791	0.2609	0.2612	0.02	99.983

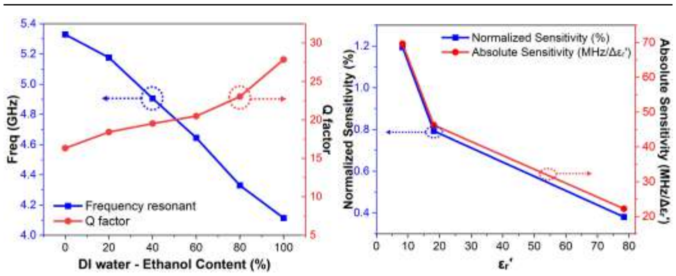

Fig. 10. (a) f_r and Q_L versus ethanol fraction; (b) S_n and S_a versus ε_r'.

The coupling gap was fixed at $s = 0.40$ mm; notch depth changed only slightly across compositions, indicating stable external coupling. Figure 10(a) plots f_r and Q_L versus ethanol concentration. As the ethanol fraction increases, f_r increases while Q_L also increases. Over 30–60% ethanol, both trends are approximately linear, enabling a first-order calibration: f_r indicates ε_r' (composition) and Q_L indicates dielectric loss. The corresponding normalized and absolute sensitivities as functions of ε_r' are summarized in Fig. 10(b).

Distinct, repeatable notches are observed for 0 to 100% ethanol (steps of 10%). Resonance shifts from 4.114 GHz (water) to 5.329 GHz (ethanol), spanning about 1.125 GHz. The largest single step, about 0.198 GHz, occurs between 60% and 70% ethanol. These spectra confirm that small permittivity differences are resolved under fixed coupling (Fig. 11).

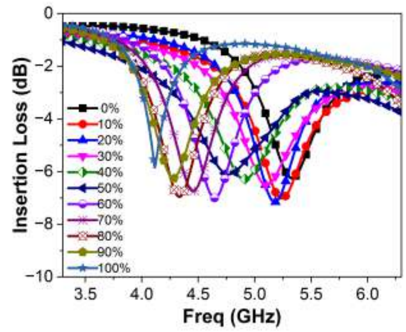

Fig. 11. Measured $|S_{21}|$ of the H-NSRR for ethanol–water mixtures (0–100% in 10% steps).

For clarity, Table IV lists the reference real permittivity ε_r' of each ethanol–water mixture used in Fig. 11. These values were computed using the well-known Lichtenecker logarithmic mixing rule for binary mixtures [47]:

$$\ln\varepsilon'_{\text{mix}} = (1-v)\ln\big(\varepsilon'_{\text{wtr}}\big) + v\ln\big(\varepsilon'_{\text{eth}}\big), \quad (11)$$

where v is the ethanol volume fraction and $\varepsilon'_{\text{wtr}}$ and $\varepsilon'_{\text{eth}}$ are the real permittivities of pure deionized water and anhydrous ethanol at 5.9 GHz. Substituting $\varepsilon'_{\text{wtr}} = 78.37$ and $\varepsilon'_{\text{eth}} = 8.27$ yields the discrete ε_r' values reported in Table IV, which serve as the reference ε_r' values used on the horizontal axis of Fig. 10(b).

TABLE IV
REAL PERMITTIVITY ε_r' OF ETHANOL–WATER MIXTURES AT 5.9 GHZ.

v	0	0.1	0.2	0.3	0.4	0.5	0.6	0.7	0.8	0.9	1.0
ε_r'	78.37	62.59	49.98	39.92	31.88	25.46	20.33	16.24	12.97	10.36	8.27

*v = volume fraction.

From these spectra, absolute and normalized sensitivities are obtained using (4) and (5), enabling fair comparison across liquids with different ε_r'. Figure 10(b) reports the absolute sensitivities: ethanol 69.64 MHz per $\Delta\varepsilon_r'$, methanol 46.26 MHz per $\Delta\varepsilon_r'$, and water 22.23 MHz per $\Delta\varepsilon_r'$. These absolute sensitivities therefore also represent the FDR values of the proposed sensor. Sensitivity decreases as ε_r' increases, consistent with nonlinear LC behavior. Over 30 to 60% ethanol, the frequency–concentration relation is about linear and the maximum normalized sensitivity reaches 1.194% near the ethanol end. To combine responsiveness and selectivity we use $\text{FoM} = S_n Q_l$, where S_n is from (5) and Q_l from the 3 dB bandwidth in (6). With near–constant notch depth, one calibration suffices; in practice, use f_r for composition and Q_l for loss without retuning the coupling.

Finally, Table V compares the proposed H-NSRR with representative planar resonant sensors for liquid dielectrics

This article has been accepted for publication in IEEE Sensors Journal. This is the author's version which has not been fully edited and content may change prior to final publication. Citation information: DOI 10.1109/JSEN.2025.3648960

TABLE V

COMPARATIVE ANALYSIS OF THE PROPOSED H-NSRR SENSOR AGAINST STATE-OF-THE-ART MICROWAVE RESONATORS FOR LIQUID DIELECTRIC CHARACTERIZATION

Ref	f_0 (GHz)	Sub.	Resonant Structure	Liquid Channel	FDR (GHz)	S (%)	E (%)	Q	Structure	V
[14]	2.44	FR-4	Waveguide + SRR	PMMA container	0.012	0.8	0.88	40	Complex	0.2
[15]	2.335	FR-4	Triple CSRR	ABS holder	0.021	0.879	< 4	120	Moderate	–
[16]	2.42	FR-4	Double SRR	Submersible	0.007	0.30	2.59	129	Simple	0.2
[17]	6.73	RO4003C	SIW + DCSRR	Glass capillary	0.012	0.18	–	–	Complex	0.2
[18]	2.46	FR-4	SIW + hex. CSRR	PDMS microfluidic	0.011	0.448	4.6	35	Complex	0.2
[19]	2.40	FR-4	MCSRR	Glass capillary	0.005	0.214	< 5	45	Moderate	0.2
[20]	2.29/3.63	RO4350B	Dual-mode SIR+IDC	PDMS microfluidic	0.080	–	2.28/5.37	–	Complex	0.1
[23]	6.21	RO4003	Meandered microstrip	Direct injection	0.040	0.64	2.0	506	Simple	–
[24]	5.76/7.85	RO4003	NID–SRR (Dual)	Contact (Droplet)	0.016/0.022	0.28/0.30	≈ 1.14	280/110	Moderate	0.1
[48]	6.00	RO4003	ML + SRR	Contact (Droplet)	0.010	0.17	N.A	38	Simple	–
[49]	3.00	RO4003	MS, LS, TS (Combined)	Contact (Droplet)	0.059	4.0	0.11	3500	Moderate	0.05
This Work	5.905	RO5880	**H-NSRR**	**PET open tray**	**0.022**	**1.194**	**1.77**	**346**	**Simple**	**0.1**

Sub. = substrate, S = sensitivity, E = error, Q = Q-factor, V = volume fraction step.

and summarizes their reported quality factors and frequency-detection resolutions (FDR). The Q values are taken as reported by the original authors; some works still define "unloaded" Q as $Q = f_0/\Delta f_{3\text{dB}}$. In this work we instead adopt the stopband-unloaded definition $Q_u = 2f_0/\Delta f_{3\text{dB}}$ with $Q_l \approx Q_u/2$ near critical coupling. The sensors in [14]–[19] generally exhibit normalized sensitivities below 1%, FDR values in the 0.005–0.021 GHz range, and unloaded Q-factors not exceeding 129, while relying on waveguide fixtures, containers, capillaries, or PDMS microfluidic channels and reporting permittivity errors of a few percent. The dual-mode RO4350B design in [20] achieves a higher FDR of 0.08 GHz but still uses a PDMS microfluidic channel and a more complex dual-resonator layout. Four recent RO4003-based resonators [23], [24], [48], [49] extend this trend, offering FDR values between 0.01 and 0.059 GHz and Q up to 3500 through meandered or multi-section SRR structures with direct-injection or droplet loading. Taken together, these works show that existing planar resonators rarely combine high normalized sensitivity, high Q, and simple non-microfluidic liquid handling within a single design. By contrast, the proposed H-NSRR combines high normalized sensitivity (1.194%), competitive FDR (0.022 GHz), and high unloaded Q in a via-less single-layer RO5880 layout with a simple 0.5-mL PET open tray. However, this open-tray interface is not suitable for sealed or continuous-flow operation and is more susceptible to evaporation for highly volatile liquids, so the sensor is best suited for benchtop batch measurements. The MS–LS–TS resonator in [49] achieves very high FDR and Q but uses a complex, container-less droplet geometry that is harder to clean and more susceptible to residue, evaporation, and manual alignment errors. These trade-offs motivate the proposed H-NSRR as an additional resonator structure for liquid permittivity characterization.

VI. CONCLUSION

This work demonstrated a single-layer, via-less H-shaped nested split-ring resonator (H-NSRR) on Rogers RO5880 operating at $5.905\,\text{GHz}$ for liquid permittivity and loss characterization. Co-localizing the fields in one gap and tuning near critical coupling yield a deep, narrow stopband with high unloaded Q-factor (Q_u approximately 346 in air). An open-top PET tray enables repeatable $0.5\,\text{mL}$ handling without microfluidics, and retrieval based on resonance-frequency shift and Q-factor variation accurately estimates ε_r' and $\tan\delta$, consistent with full-wave simulation and probe measurements. The H-NSRR thus provides a compact, sensitive platform (maximum normalized sensitivity 1.194%) for reliable small-volume microwave liquid testing; future work will develop a differential H-NSRR to mitigate cross-sensitivity and environmental effects while further reducing sample volume and improving thermal stability.

REFERENCES

[1] M. Bazgir and A. Sheikhi, "High q-factor compact permittivity sensor based on coupled srr-elc metamaterial element and metasurfaces shield," *IEEE Sensors Journal*, vol. 24, no. 4, pp. 4424–4431, 2024.

[2] S. Kiani, P. Rezaei, and M. Fakhr, "A cpw-fed wearable antenna at ism band for biomedical and wban applications," *Wireless Networks*, vol. 27, no. 1, pp. 735–745, 2021.

[3] Y. Yakhlef *et al.*, "Highly sensitive microwave sensor based on planar resonator arrangement for dielectric material characterization," *IEEE Sensors Journal*, 2024.

[4] U. Ali *et al.*, "A novel fractal hilbert curve-based low-cost and highly sensitive microwave sensor for dielectric characterization of liquid materials," *IEEE Sensors Journal*, vol. 23, no. 20, pp. 23 950–23 957, 2023.

[5] R. A. Alahnomi *et al.*, "Review of recent microwave planar resonator-based sensors: Techniques of complex permittivity extraction, applications, open challenges and future research directions," *Sensors*, vol. 21, no. 7, p. 2267, 2021.

[6] M. Abdolrazzaghi, V. Nayyeri, and F. Martin, "Techniques to improve the performance of planar microwave sensors: A review and recent developments," *Sensors*, vol. 22, no. 18, p. 6946, 2022.

[7] W.-S. Zhao *et al.*, "Microwave planar sensors for fully characterizing magneto-dielectric materials," *IEEE Access*, vol. 8, pp. 41 985–41 999, 03 2020.

[8] T. Alam and M. Cheffena, "Integrated microwave antenna/sensor for sensing and communication applications," *IEEE Transactions on Microwave Theory and Techniques*, vol. 70, no. 11, pp. 5289–5300, 2022.

[9] A. Kandwal *et al.*, "Electromagnetic wave sensors for noninvasive blood glucose monitoring: Review and recent developments," *IEEE Transactions on Instrumentation and Measurement*, vol. 72, pp. 1–15, 2023.

[10] A. K. Jha *et al.*, "A highly sensitive planar microwave sensor for detecting direction and angle of rotation," *IEEE Transactions on Microwave Theory and Techniques*, vol. 68, no. 4, pp. 1598–1609, 2020.

[11] A. B. Bilgin and P. Basaran, "Microwave sensing and imaging technology in food applications: A comprehensive review," *Comprehensive Reviews in Food Science and Food Safety*, vol. 24, no. 4, p. e70220, 2025.

[12] C. Cho *et al.*, "Passive wireless frequency doubling antenna sensor for strain and crack sensing," *IEEE Sensors Journal*, vol. 16, no. 14, pp. 5725–5733, 2016.

[13] O. Malyuskin, "Microplastic detection in soil and water using resonance microwave spectroscopy: A feasibility study," *IEEE Sensors Journal*, vol. 20, no. 24, pp. 14 817–14 826, 2020.

[14] Y. Zhang *et al.*, "High sensitivity detection of ethanol solution based on waveguide resonant cavity combined with metamaterials," *Measurement*, vol. 225, p. 114030, 2024.

[15] A. Buragohain, A. T. T. Mostako, and G. S. Das, "Low-cost csrr based sensor for determination of dielectric constant of liquid samples," *IEEE Sensors Journal*, vol. 21, no. 24, pp. 27 450–27 457, 2021.

[16] S.-Y. Jang and J.-R. Yang, "Double split-ring resonator for dielectric constant measurement of solids and liquids," *Journal of Electromagnetic Engineering and Science*, vol. 22, no. 2, pp. 122–128, 2022.

[17] V. García, Y. Campos-Roca, and A. G. García, "Differential sensors in substrate integrated waveguide technology loaded with complementary split-ring resonators for liquid characterization," *IEEE Sensors Journal*, vol. 24, no. 1, pp. 270–277, 2023.

[18] X. Han *et al.*, "Highly integrated improved hexagonal csrr-based fluid sensor for complex dielectric parameter detection," *IEEE Sensors Journal*, vol. 24, no. 13, pp. 20 559–20 570, 2024.

[19] A. Javed *et al.*, "A low-cost multiple complementary split-ring resonator-based microwave sensor for contactless dielectric characterization of liquids," *IEEE Sensors Journal*, vol. 20, no. 19, pp. 11 326–11 334, 2020.

[20] W. Ye *et al.*, "An ultrahigh-sensitivity dual-mode microwave sensor for microfluidic applications," *IEEE Microwave and Wireless Technology Letters*, vol. 33, no. 7, pp. 1082–1085, 2023.

[21] J. Ma *et al.*, "Complex permittivity characterization of liquid samples based on a split ring resonator (srr)," *Sensors*, vol. 21, no. 10, p. 3385, 2021.

[22] Z. Li *et al.*, "High-sensitivity differential sensor for characterizing complex permittivity of liquids based on lc resonators," *Sensors*, vol. 24, no. 15, p. 4877, 2024.

[23] S. Kiani, P. Rezaei, and M. Fakhr, "Real-time measurement of liquid permittivity through label-free meandered microwave sensor," *IETE Journal of Research*, vol. 70, no. 5, pp. 4606–4616, 2024.

[24] S. Kiani, P. Rezaei, and M. Navaei, "Dual-sensing and dual-frequency microwave srr sensor for liquid samples permittivity detection," *Measurement*, vol. 160, p. 107805, 2020.

[25] C. Wang *et al.*, "High-accuracy complex permittivity characterization of solid materials using parallel interdigital capacitor-based planar microwave sensor," *IEEE Sensors Journal*, vol. 21, no. 5, pp. 6083–6093, 2020.

[26] C. Su and G. Liu, "High sensitivity cpw microwave sensor based on ocsrr and ide structure for permittivity characterization," *IEEE Sensors Journal*, 2025.

[27] Z. R. Omam *et al.*, "Simple and high-sensitivity dielectric constant measurement using a high-directivity microstrip coupled-line directional coupler," *IEEE Transactions on Microwave Theory and Techniques*, vol. 70, no. 8, pp. 3933–3942, 2022.

[28] W. Qi *et al.*, "A microwave measurement system based on high-sensitivity stepped impedance resonators (sirs) for testing permittivity of dielectric materials and liquid samples," *IEEE Sensors Journal*, 2025.

[29] Y. Cao *et al.*, "Research on a high-sensitivity asymmetric metamaterial structure and its application as microwave sensor," *Scientific Reports*, vol. 12, no. 1, p. 1255, 2022.

[30] C.-F. Liu, M.-H. Wang, and L.-S. Jang, "Microfluidics-based hairpin resonator biosensor for biological cell detection," *Sensors and Actuators B: Chemical*, vol. 263, pp. 129–136, 2018.

[31] G. Chen *et al.*, "A microwave sensing system based on reflective rf oscillator and high-sensitivity coupled-line sensor for extracting permittivity of liquid samples," *IEEE Sensors Journal*, 2024.

[32] M. Baghelani, O. Hasan-Nejad, and M. Daneshmand, "Highly sensitive microwave sensor for high precision sensing of water contamination in mineral oil," *IEEE Sensors Journal*, vol. 21, no. 12, pp. 13 247–13 254, 2021.

[33] A. Buragohain *et al.*, "Highly sensitive differential hexagonal split ring resonator sensor for material characterization," *Sensors and Actuators A: Physical*, vol. 363, p. 114704, 2023.

[34] S. Mohammadi *et al.*, "High-resolution, sensitivity-enhanced active resonator sensor using substrate-embedded channel for characterizing low-concentration liquid mixtures," *IEEE Transactions on Microwave Theory and Techniques*, vol. 70, no. 1, pp. 576–586, 2021.

[35] W. Ye *et al.*, "An improved split-ring resonator-based sensor for microfluidic applications," *Sensors*, vol. 22, no. 21, p. 8534, 2022.

[36] J. Chen *et al.*, "Multimode fano resonances sensing based on a non-through mim waveguide with a square split-ring resonance cavity," *Biosensors*, vol. 12, no. 5, p. 306, 2022.

[37] H. N. Anggradinata and M. Asvial, "Multifunctional dual-band microwave sensor for the detection of liquid permittivity and solid displacement," *Progress In Electromagnetics Research C*, vol. 152, pp. 131–141, 2025.

[38] G. Yang *et al.*, "Theoretical analysis for high-sensitivity sensor," pp. 280–282, 2022.

[39] S. I. Huq, G. Xiao, and S. Bhadra, "Printed split ring resonator based microwave sensor on biodegradable substrate for dielectric characterization," *Sensors and Actuators A: Physical*, p. 116856, 2025.

[40] M. Abdolrazzaghi, M. Daneshmand, and A. K. Iyer, "Strongly enhanced sensitivity in planar microwave sensors based on metamaterial coupling," *IEEE Transactions on Microwave Theory and Techniques*, vol. 66, no. 4, pp. 1843–1855, 2018.

[41] J. Zhou, T. Koschny, and C. Soukoulis, "Magnetic and electric excitations in split ring resonators," *Optics Express*, vol. 15, pp. 17 881–17 890, 12 2007.

[42] A. Khanna and Y. Garault, "Determination of loaded, unloaded, and external quality factors of a dielectric resonator coupled to a microstrip line," *IEEE Transactions on Microwave Theory and Techniques*, vol. 31, no. 3, pp. 261–264, 2003.

[43] W. Liu *et al.*, "Improve planar multiple split-ring sensor for microwave detection applications," *Sensors and Actuators A: Physical*, vol. 297, p. 111542, 2019.

[44] A. Kik, "Complex permittivity measurement using a ridged waveguide cavity and the perturbation method," *IEEE Transactions on Microwave Theory and Techniques*, vol. 64, no. 11, pp. 3878–3886, 2016.

[45] A. Alhegazi *et al.*, "Novel technique of gap waveguide cavity resonator sensor with high resolution for liquid detection," *International Journal of Antennas and Propagation*, vol. 2022, no. 1, p. 2401586, 2022.

[46] N. Abd Rahman *et al.*, "Liquid permittivity sensing using teeth gear-circular substrate integrated waveguide," *IEEE Sensors Journal*, vol. 22, no. 12, pp. 11 690–11 697, 2022.

[47] A. Rasoulzadeh, C. Ghobadi, and J. Nourinia, "A compact differential microwave fluid sensor for permittivity measurement of ethanol-water solution," *IEEE Sensors Journal*, 2025.

[48] M. Navaei, P. Rezaei, and S. Kiani, "Microwave split ring resonator sensor for determination of the fluids permittivity with measurement of human milk samples," *Radio Science*, vol. 57, no. 7, pp. 1–11, 2022.

[49] M. Navaei, P. Rezaei, and S. Kiani, "Measurement of low-loss aqueous solutions permittivity with high detection accuracy by a contact and free-label resonance microwave sensor," *International Journal of Communication Systems*, vol. 36, no. 5, p. e5417, 2023.

This article has been accepted for publication in IEEE Sensors Journal. This is the author's version which has not been fully edited and content may change prior to final publication. Citation information: DOI 10.1109/JSEN.2025.3648960

MUHAMAD ZAKI ABDUL RAHMAN Received the B.Eng. degree in Electrical Engineering from Kolej Universiti Teknologi Tun Hussein Onn, Malaysia, in 2002, and the M.Eng. degree in Electronic Engineering (Electronic Systems) from Universiti Teknikal Malaysia Melaka (UTeM), Melaka, Malaysia, in 2013. He is a Lecturer with the Department of Electrical Engineering, Politeknik Ungku Omar, Malaysia, and is currently pursuing the Ph.D. degree with the Faculty of Electronic and Computer Engineering Technology (FTKEK), UTeM. His research interests include microwave resonator sensors and planar RF structures.

MUHAMMAD IDZDIHAR IDRIS Received the B.Eng. degree from Hiroshima University, Japan, the M.Sc. degree from Universiti Kebangsaan Malaysia (UKM), Malaysia, and the Ph.D. degree from Newcastle University, U.K., in 2010, 2012, and 2018, respectively. He is currently an Associate Professor with Universiti Teknikal Malaysia Melaka (UTeM), Melaka, Malaysia. His research interests include the fabrication and characterization of semiconductor devices, including MOSFETs, solar cells, and gas sensors.

NAZRIN HAZIQ JEMALUDIN Received the B.Eng. degree in Electronic Engineering from Universiti Teknikal Malaysia Melaka (UTeM), Melaka, Malaysia. He is currently pursuing the M.Sc. degree with the Centre for Telecommunication Research and Innovation (CeTRI), Faculty of Electronic and Computer Engineering, UTeM. His research interests include antennas, microwave engineering, and Internet-of-Things-based sensing and wireless applications.

MD RAZIP BIN MAT Received the B.Eng. degree in Electrical Engineering from Kolej Universiti Teknologi Tun Hussein Onn, Malaysia, in 2003, and the M.Eng. degree in Electronic Engineering (Electronic Systems) from Universiti Teknikal Malaysia Melaka (UTeM), Melaka, Malaysia, in 2013. He is currently a Lecturer with Politeknik Ungku Omar, Ipoh, Malaysia. His research interests include microwave resonator sensors and planar RF structures.

SAFPBRI JOHARI Received the B.S. degree from the Faculty of Electrical Engineering, Universiti Teknologi Malaysia, Malaysia, in 2014, and the M.S. degree from the Faculty of Electrical Engineering, Universiti Teknologi MARA, Malaysia, in 2018. He is currently pursuing the Ph.D. degree with the Faculty of Electronic Engineering and Technology, Universiti Malaysia Perlis, Malaysia. His research interests focus on reconfigurable intelligent surfaces and antenna design.

SYAH ALAM (Member, IEEE) Received the Bachelor of Education (S.Pd.) degree in Electrical Engineering from Universitas Pendidikan Indonesia (UPI), Indonesia, in 2010, the M.Eng. degree in Electrical Telecommunication Engineering from Universitas Trisakti, Indonesia, in 2012, and the Ph.D. degree in Electronic Engineering (RF and microwave) from Universiti Teknikal Malaysia Melaka (UTeM), Melaka, Malaysia, in 2024. His research interests include microstrip antennas and microwave sensors for various applications.

ZAHRILADHA ZAKARIA (Senior Member, IEEE) Received the B.Eng. and M.Eng. degrees in Electrical and Electronic Engineering from Universiti Teknologi Malaysia, Malaysia, in 1998 and 2004, respectively, and the Ph.D. degree in Electrical and Electronic Engineering from the Institute of Microwaves and Photonics, University of Leeds, Leeds, U.K., in 2010. He is currently the Deputy Vice-Chancellor (Research and Innovation) and a Professor with the Microwave Research Group (MRG), Faculty of Electronic and Computer Engineering, Universiti Teknikal Malaysia Melaka (UTeM), Melaka, Malaysia. His research interests include microwave devices and resonators, antennas, energy harvesting, and sensing.

Alam, Syah

Universitas Trisakti, Jakarta, Indonesia • Scopus ID: 57191903622 • 0000-0002-0162-8364

Show all information

353
Citations by **266** documents

77
Documents

11
h-index

Set alert   Save to list   Edit profile   More

Documents (77)   Impact   Cited by (266)   Preprints (1)   Co-authors (130)   Topics (15)   Beta Awarded grants (0)

You can view, sort, and filter all of the documents in search results format.

Export all   Save all to list   Sort by Date (newest)

Article

A Single-Port Microwave Sensor Based on Interdigital Capacitor and Electromagnetic Coupled Structure for Permittivity Detection of Vegetables Materials

0
Citations

Sari, F.K., Alam, S., Surjati, I., ... Zakaria, Z., Shairi, N.A.
Sensing and Imaging, 2026, 27(1), 7
Show abstract Full text Related documents

Article
Independent and asymmetric coupling structure for integrated dual-band bandpass filter with microwave microfluidic milk sensor
0 Citations
Firmansyah, T., Praptodiyono, S., Muttakin, I., ... Iqbal, M., Nugraha
AEU International Journal of Electronics and Communications, 2026, 206, 156186
Show abstract Full text Related documents

Article
Fabric-Based Metamaterial-Integrated CPW Antenna for Microwave Tumor Sensing
0 Citations
Abd Razak, I.S., Al-Gburi, A.J.A., Meor Said, M.A., Alam, S., Zakaria, Z.
IEEE Sensors Journal, 2026, 26(3), pp. 3944–3953
Show abstract Full text Related documents

Article • Article in Press
High-Q H-Shaped Nested Split-Ring Resonator Sensor for Liquid Complex-Permittivity Characterization
0 Citations
Rahman, M.Z.A., Idris, M.I., Jemaludin, N.H., ... Alam, S., Zakaria, Z.
IEEE Sensors Journal, 2026
Show abstract Full text Related documents

Article

Application of LT Code with BCH Precode for Wireless Body Area Network

Sari, L., Alam, S., Mardian, R.D., Surjati, I.

Journal of Electrical and Electronics Engineering, 2025, 18(2), pp. 63–68

Show abstract Full text Related documents

Article

Multifunctional microwave-plasmonic microfluidic sensor utilizing gold nanoparticles embedded in multilayered ring resonator

Firmansyah, T., Alfanz, R., Denny, Y.R., ... Wibisono, G., Kondoh, J.

Sensors and Actuators A Physical, 2025, 385, 116275

Show abstract Full text Related documents

Article • *Open access*

SAR Distribution with Different Water Bolus Shapes for Hyperthermia Breast Cancer Treatment

Hassan, M.M., Lias, K., Buniyamin, N., ... Basri, H.M., Alam, S.

Journal of Advanced Research in Fluid Mechanics and Thermal Sciences, 2025, 128(1), pp. 32–47

Show abstract Full text Related documents

Article • *Open access*

A Broadband Half-Mode Substrate Integrated Waveguide Cavity Antenna with Triple Resonances

Astuti, D.W., Majid, H.A., Alam, S., Setyawan, A.

Progress in Electromagnetics Research C, 2025, 152, pp. 55–66

Show abstract Full text Related documents

Article • *Open access*

Broadband HMSIW antenna using a demi hexagonal ring slot for X-band application

Astuti, D.W., Muslim, M., Umaisaroh, U., ... Alam, S., Rahayu, Y.

Sinergi Indonesia, 2025, 29(1), pp. 73–82

Show abstract Full text Related documents

Article

A Fabric-Based Double Rectangular Complementary Split Ring Resonator for Wideband Applications

1 Citations

Abd. Razak, I.S., Zakaria, Z., Al-Gburi, A.J.A., ... Alam, S., Palandoken, M.

Progress in Electromagnetics Research C, 2025, 157, pp. 147–158

Show abstract Full text Related documents

View all references

Document & citation trends

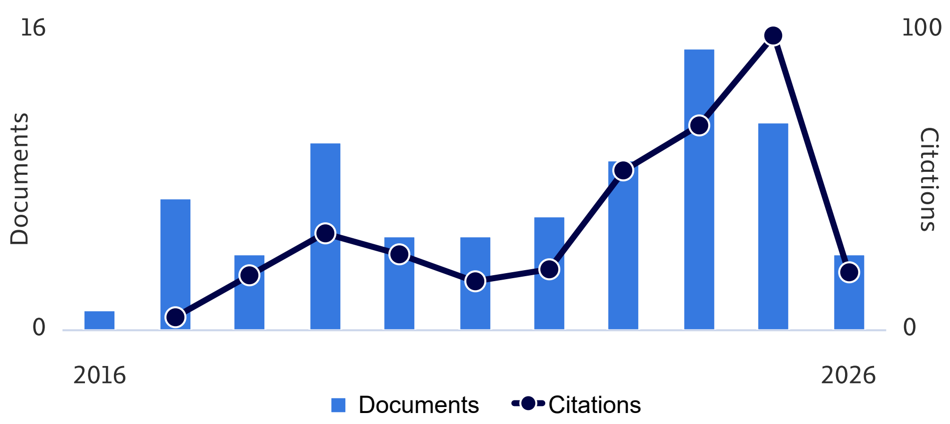

Citation overview   Analyze author output

Author Position for 2015 - 2024

First author 49%

29 Documents

5 Average citations

0.689 FWCI

Last author 18%

Co-author 33%

Single author 0%

Show author position details

Back to top